RESEARCH ARTICLE

Key Points:
- A floe-scale survey shows that Antarctic pack ice transmits <0.1% of solar radiation during early spring
- Freeboard and flooding dominate the spatial variability of the under-ice light regime
- In contrast to Arctic sea ice, the heterogeneous snow on Antarctic pack ice obscures a direct correlation between the under-ice light field and snow depth

Supporting Information:
- Supporting Information S1
- Figure S1
- Figure S2
- Figure S3

Correspondence to:
S. Arndt,
stefanie.arndt@awi.de

Influence of snow depth and surface flooding on light transmission through Antarctic pack ice

Stefanie Arndt[1], Klaus M. Meiners[2,3], Robert Ricker[1,4], Thomas Krumpen[1], Christian Katlein[1], and Marcel Nicolaus[1]

[1]Alfred-Wegener-Institut Helmholtz-Zentrum für Polar- und Meeresforschung, Bremerhaven, Germany, [2]Australian Antarctic Division, Department of the Environment and Energy, Kingston, Tasmania, Australia, [3]Antarctic Climate and Ecosystems Cooperative Research Centre, University of Tasmania, Hobart, Tasmania, Australia, [4]Univ. Brest, CNRS, IRD, Ifremer, Laboratoire d'Ocanographie Physique et Spatiale (LOPS), IUEM, Brest, France

Abstract Snow on sea ice alters the properties of the underlying ice cover as well as associated physical and biological processes at the interfaces between atmosphere, sea ice, and ocean. The Antarctic snow cover persists during most of the year and contributes significantly to the sea-ice mass due to the widespread surface flooding and related snow-ice formation. Snow also enhances the sea-ice surface reflectivity of incoming shortwave radiation and determines therefore the amount of light being reflected, absorbed, and transmitted to the upper ocean. Here, we present results of a case study of spectral solar radiation measurements under Antarctic pack ice with an instrumented Remotely Operated Vehicle in the Weddell Sea in 2013. In order to identify the key variables controlling the spatial distribution of the under-ice light regime, we exploit under-ice optical measurements in combination with simultaneous characterization of surface properties, such as sea-ice thickness and snow depth. Our results reveal that the distribution of flooded and nonflooded sea-ice areas dominates the spatial scales of under-ice light variability for areas smaller than 100 m-by-100 m. However, the heterogeneous and highly metamorphous snow on Antarctic pack ice obscures a direct correlation between the under-ice light field and snow depth. Compared to the Arctic, light levels under Antarctic pack ice are extremely low during spring (<0.1%). This is mostly a result of the distinctly different dominant sea ice and snow properties with seasonal snow cover (including strong surface melt and summer melt ponds) in the Arctic and a year-round snow cover and widespread surface flooding in the Southern Ocean.

1. Introduction

Snow on sea ice plays a crucial role for interactions between the ocean and atmosphere within the polar climate system and is a key driver of polar marine ecosystem function, especially in the year-round snow-covered Antarctic sea-ice zone [*Massom et al.*, 2001; *Massom and Stammerjohn*, 2010]. Snow contributes substantially to the sea-ice mass balance of Antarctic sea ice as the heavy snow load depresses the ice below the water level, causing flooding and the formation of snow-ice during the subsequent refreezing of the formed slush [*Arrigo*, 2014; *Eicken et al.*, 1994; *Haas et al.*, 2001]. In addition, superimposed ice, forming during summer when percolating melt water refreezes at the snow/ice interface, adds to the sea-ice mass [*Haas*, 2001; *Nicolaus et al.*, 2003]. The snow cover also determines the surface energy budget of the ice-covered ocean by influencing the amount of shortwave radiation being reflected, absorbed, and transmitted into the upper ocean [*Brandt et al.*, 2005; *Massom et al.*, 2001]. Snow extinction coefficients are more than one order of magnitude larger than those of bare sea ice, and snow albedo can be almost twice as large as that of ice [*Grenfell and Maykut*, 1977; *Perovich*, 1996].

The horizontal and vertical distribution of solar radiation under sea ice impacts not only the physical properties but also biological processes and biogeochemical fluxes in the sea ice and the uppermost ocean [*Arrigo et al.*, 2012; *Fritsen et al.*, 2011; *Perovich*, 1996, 2007]. Due to their different spectral absorption characteristics, snow, sea ice, sea water, biota, sediments, and other impurities affect the spectral composition of the light penetrating from the atmosphere into the ocean [*Belzile et al.*, 2000; *Mundy et al.*, 2005; *Perovich*, 1996; *Uusikivi et al.*, 2010]. The spectral composition of transmitted under-ice irradiance measurements has been used to estimate biota (e.g., ice algal biomass as Chlorophyll *a*, Chl *a*) and snow depth in Arctic sea ice

[*Campbell et al.*, 2015; *Mundy et al.*, 2007]. The latter is also of high interest in Antarctic pack ice, since comprehensive snow measurements from space and/or in situ measurements are lacking. In a recent study, *Melbourne-Thomas et al.* [2015] applied normalized difference indices of under-ice irradiance spectra to develop algorithms to estimate snow depth in Antarctic pack ice.

Optical properties of Arctic sea ice, in particular the effects of spatial variations of snow and sea-ice surface properties on the under-ice light regime, are relatively well studied [*Frey et al.*, 2011; *Katlein et al.*, 2015; *Light et al.*, 2008; *Nicolaus et al.*, 2012; *Perovich*, 1996; *Perovich et al.*, 1998]. Investigations of the under-ice light regime in the ice-covered Arctic Ocean have been carried out as either local point measurements using radiometers mounted to retractable L-shaped arms or with instrumented Remotely Operated Vehicles (ROV) which allow investigations on larger spatial scales ($>$1000 m^2) [*Nicolaus et al.*, 2012; *Perovich*, 1996; *Perovich et al.*, 2011]. The results reveal strong correlation between the spatial variations in light transmittance of Arctic sea ice, and the prevalent ice type (first-year/multiyear ice) and its surface properties (e.g., melt pond coverage, snow cover), respectively. On large scales, the ice thickness distribution is the main driver of the spatial variability in the under-ice light field [*Katlein et al.*, 2015]. Using these relationships, *Arndt and Nicolaus* [2014] were able to derive a seasonality for under-ice radiation for the Arctic Ocean based on ice type and surface characteristics.

In contrast, the information on the optical properties of Antarctic sea ice, especially free-drifting pack ice, remains extremely sparse [*Fritsen et al.*, 2011; *Michael and Higgins*, 2014]. To our knowledge, only point measurements of under-ice irradiance spectra (L-arm measurements) were collected during field campaigns, e.g., the Winter Weddell Outflow Study (WWOS) in the Weddell Sea in austral summer 2006 [*Lemke*, 2009], the Sea Ice Mass Balance in the Antarctic (SIMBA) campaign in the Bellingshausen Sea in 2007 [*Fritsen et al.*, 2011], followed by two Sea Ice Physics and Ecosystems Experiment voyages (SIPEX1 and SIPEX-2) in East Antarctica in austral spring 2007 and 2012 [*Meiners et al.*, 2016; *Worby et al.*, 2011].

In this case study, we present the first data on the spatial variability of sea-ice physical parameters and their influence on solar radiation under Antarctic pack ice. Under-ice solar radiation was measured with an ROV instrumented with a radiometer and sensors supporting under-ice navigation. In order to identify key processes controlling the spatial distribution of the under-ice light field in an area of approximately 100 m-by-100 m, we combine under-ice optical measurements with coincident characterization of the surface properties, such as sea-ice thickness and snow depth. Results are discussed in context of recent studies on the spatial variability of the Arctic under-ice light field focusing on the distinctly differing surface properties between the northern (e.g., summer melt ponds) and southern (e.g., year-round snow cover, surface flooding) hemisphere sea-ice covers.

2. Data and Methods

2.1. Study Site and Measurements

ROV measurements were carried out during the expedition ANT-29/7 of the German ice-breaker R/V *Polarstern* during the "Winter studies on sea ice and key species" (WISKEY) project in the northern Weddell Sea (Figure 1) [*Meyer and Auerswald*, 2014]. The described sea-ice floe was surveyed during the second ice camp at about 60.78°S and 26.36°W. Measurements with an ROV were carried out from 18 to 26 September 2013 on a 100 m-by-100 m grid during 17 dives. The sea-ice surface conditions were stable during this period, which allows merging all under-ice measurements into one data set for the following analyses (S1). The ROV was instrumented with an upward-looking RAMSES-ACC (Advanced Cosine Collector) spectral radiometer (Trios GmbH, Rastede, Germany) to measure downwelling planar under-ice spectral irradiance (320–950 nm) and an upward-looking Valeport VA500 altimeter to measure the distance between the ROV and the bottom of the sea ice. The ROV position was determined using a long baseline positioning system (LBL) consisting of a Woods Hole Oceanographic Institution (WHOI) FSK micromodem equipped with an ITC 3013 transducer (mounted on the ROV) and interrogating four Benthos XT-6001 transponders (15 m depth) which were coupled to surface GPS units and spaced around the survey site in a rectangle with 400 m side length [e.g., *Williams et al.*, 2013]. The surface GPS were also used for precise coregistration of temporally displaced surface measurements using GPS equipped snow and total-ice-thickness instruments, i.e., accounting for ice-floe drift and rotation in-between ROV- and surface measurements [e.g., *Williams et al.*, 2013]. Incident solar irradiance was measured synchronously with a reference RAMSES-ACC sensor next to
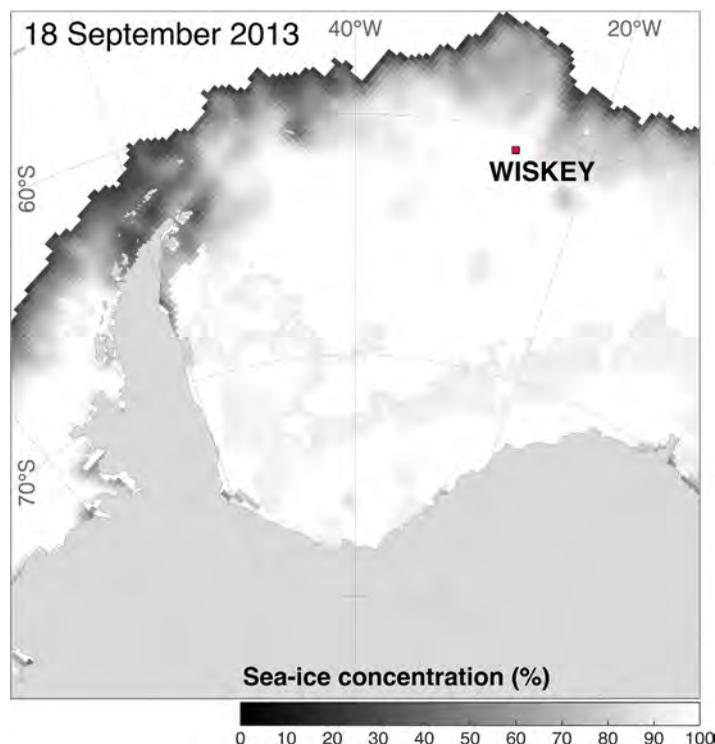
Figure 1. Ice-station location sampled during voyage ANT-29/7 (PS81, WISKEY) with R/V Polarstern in the Weddell Sea from 18 to 26 September 2013. The background image shows the sea-ice concentration on 18 September 2013 provided by www.meereisportal.de.

the ROV grid on the sea-ice surface. Surface measurements of sea-ice thickness and snow depth were conducted after the ROV measurements to avoid disturbance of the snow cover.

For all presented broadband values, the hyperspectral measurements were integrated over the range of Photosynthetically Active Radiation (PAR) from 400 to 700 nm after interpolation to a spectral resolution of 1 nm [*Nicolaus et al.*, 2010]. Details on the processing of the optical data and the calculation of the transmittance as a ratio of under-ice irradiance and incoming solar irradiance are described in *Nicolaus et al.* [2010] and *Nicolaus and Katlein* [2013]. Instead of correcting all under-ice irradiance data to the ice-ocean interface, only data points with a maximum ROV-ice distance of 2 m were taken into account. This resulted in a total of 4586 valid under-ice irradiance and light transmission spectra. To account for multiple sampling due to overlapping ROV tracks and position errors, all data were regridded by averaging all measurements taken within a grid cell of 2 m-by-2 m. All grid cells overlap for 1m translating to an effective grid resolution of 1 m (running mean).

In addition to the optical measurements with the ROV, total sea-ice thickness (sea-ice thickness plus snow depth) was measured on the entire ice floe and particularly on the ROV survey grid with a ground-based multifrequency electromagnetic induction instrument (GEM-2, Geophex Ltd.) [*Hunkeler et al.*, 2016]. The instrument was mounted on a modified plastic sled and pulled over the snow surface. A GPS-equipped Magna Probe (Snow Hydro, Fairbanks, AK, USA) was operated simultaneously in order to obtain snow depth along the GEM-2 tracks. Snow depth measurements were taken every 1.5–2.5 m along the track. Sea-ice thickness was then calculated as the difference of total sea-ice thickness and snow depth. Both sea-ice thickness and snow depth measurements were interpolated to the locations of the under-ice measurements using nearest-neighbor resampling.

2.2. Data Analyses

2.2.1. Ice Freeboard and Flooding

Ice freeboard, F, is controlled by the difference between sea-ice buoyancy and snow load. Especially for the ice-covered Southern Ocean, two typical states of sea ice must be distinguished, one with the snow/ice interface above the sea level (positive freeboard, Figure 2a), and the other with the snow/ice interface below the sea level (negative freeboard, Figure 2b). For the case of a positive freeboard (Figure 2a), the ice buoyancy of floating sea ice is defined by the density of sea ice, ρ_i, the density of seawater, ρ_w, and the sea-ice thickness, I, while the snow load is calculated from the density of snow, ρ_s, and the snow depth, S [*Lange et al.*, 1990; *Sturm and Massom*, 2010]. Assuming a hydrostatic equilibrium for a floating snow-covered sea-ice floe, ice freeboard, F, can be calculated by

$$F = \frac{I \cdot (\rho_w - \rho_i) - S \cdot \rho_S}{\rho_w}. \tag{1.1}$$
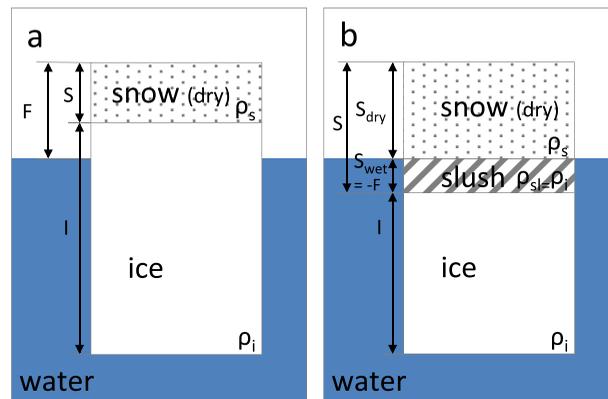
Figure 2. Two typical states of Antarctic sea ice. (a) Positive freeboard with the snow/ice interface above the sea level. (b) Negative freeboard with the snow/ice interface below the sea level. The flooded snow (slush) is referred to as (negative) freeboard and is assumed to have the same density as sea ice.

A negative freeboard is associated with flooding at the snow/ice interface leading to the formation of slush and snow-ice at the snow/ice interface (Figure 2b), which can therefore be assumed to have the same density as sea ice [*Knight*, 1988]. Therefore, as soon as F gets negative (equation (1.1)), the slush layer thickness, and thus the freeboard is calculated as

$$S_{wet} = -F = S + \frac{I+S}{1+\frac{\rho_s}{\rho_w - \rho_i}}. \quad (1.2)$$

In this study, constant densities for seawater, sea ice, and snow of 1023.9, 915.1, and 300 kg m^{-3} are assumed, respectively [*Yi et al.*, 2011].

2.2.2. Extinction Coefficient

Extinction coefficients describe the attenuation of light penetrating from the air-snow/ice interface to the ice-ocean interface due to scattering and absorption [*Perovich*, 1996]. Spectrally resolved bulk extinction coefficients κ_d were calculated from light transmittance, T, and total sea-ice thickness (ice thickness plus snow depth), I+S,

$$\kappa_d(\lambda) = -\frac{\ln(T(\lambda))}{I+S}. \quad (2)$$

To investigate the difference of light attenuation characteristics of snow and sea ice, we fitted a multiple exponential model to estimate single ice and snow extinction coefficients, κ_{ice} and κ_{snow}, dependent on the respective ice thickness, I, and snow depth, S,

$$T(I, S, \lambda) = \exp(-\kappa_{ice}(\lambda) \cdot I) \cdot \exp(-\kappa_{snow}(\lambda) \cdot S). \quad (3.1)$$

Taking into account an additional flooding layer at the snow/ice interface, and therefore extending the multiple exponential model toward a third component for flooded snow (F, κ_{slush}), leads to:

$$\tau(I, S, F, \lambda) = \exp(-\kappa_{ice}(\lambda) \cdot I) \cdot \exp(-\kappa_{snow}(\lambda) \cdot S) \cdot \exp(-\kappa_{slush}(\lambda) \cdot |F|). \quad (3.2)$$

To solve equations (3.1) and (3.2) for the attenuation coefficients, the *Curve fitting* toolbox of the statistical software *Matlab* was used by applying a multiple nonlinear least square regression algorithm. Uncertainties are given as a function of the accuracy of the retrieved sea-ice thickness, which is given as 0.1 m for the used GEM-2 [*Hunkeler et al.*, 2015]. The contribution of the snow-depth uncertainty as well as the uncertainties of the applied densities of snow, sea ice, and the slush layer are proved to be small compared to the contribution of the sea-ice thickness retrieval.

2.2.3. Normalized Difference Index (NDI)

Normalized difference indices (NDIs) of under-ice irradiance spectra have been used to investigate the relationship between e.g., snow depth and transmitted spectra under sea ice. Following *Mundy et al.* [2007], NDIs were calculated for all wavelength combinations (400–700 nm) of λ_1 and λ_2 from transmitted under-ice irradiance spectra $E_d(\lambda)$, through the entire snow and ice column, according to

$$NDI = \frac{E_d(\lambda_1) - E_d(\lambda_2)}{E_d(\lambda_1) + E_d(\lambda_2)}. \quad (4)$$

The subsequent spectral correlation surfaces were constructed from the Pearson's correlation coefficients calculated from correlations of NDIs for each wavelength pair and snow depth [*Mundy et al.*, 2007].

3. Results

3.1. Physical Properties of the Ice Floe and Their Distribution Functions

The surveyed large ice floe (>1 km^2) was a compound first-year sea-ice floe with significant deformation and variable snow cover. GEM2-based ice thickness and Magna Probe snow-depth surveys for the entire

**Table 1.** Summary Statistics for Measured and Calculated Physical Sea-Ice Parameters for the PS81 Data Set, Nonflooded Grid Cells Only (Positive Freeboard), and Flooded Grid Cells Only (Negative Freeboard)[a]

Parameter		All Data Points ($n = 4595$)	Nonflooded Data Points Only ($n = 1080$)	Flooded Data Points Only ($n = 3515$)
Sea-ice thickness (m)		0.93 ± 0.45	1.42 ± 0.51	0.78 ± 0.30
Snow depth (m)		0.39 ± 0.13	0.30 ± 0.12	0.42 ± 0.12
Ice freeboard (m)		-0.08 ± 0.10	0.05 ± 0.04	-0.12 ± 0.07
Light transmittance	Mean	0.0024 ± 0.0030	0.0019 ± 0.0025	0.0026 ± 0.0031
	Mode	0.0008	0.0008	0.0008
Bulk extinction coefficient (m^{-1})	Mean	5.52 ± 1.66	4.49 ± 1.54	5.84 ± 1.56
	Mode	5.5	3.75	5.5
Extinction coefficient (m^{-1})	Ice	6.829 ± 0.045	1.264 ± 0.133	2.06 ± 0.97
	Snow	7.737 ± 0.049	31.76 ± 0.69	31.22 ± 0.53
	Slush			6.21 ± 3.23

[a]Reported values are mean values $\pm$ its standard deviation or mode values. Extinction coefficients are estimated as bulk-extinction coefficients according to equation (2) and separated for ice and snow applying an exponential fit according to equation (3.1).
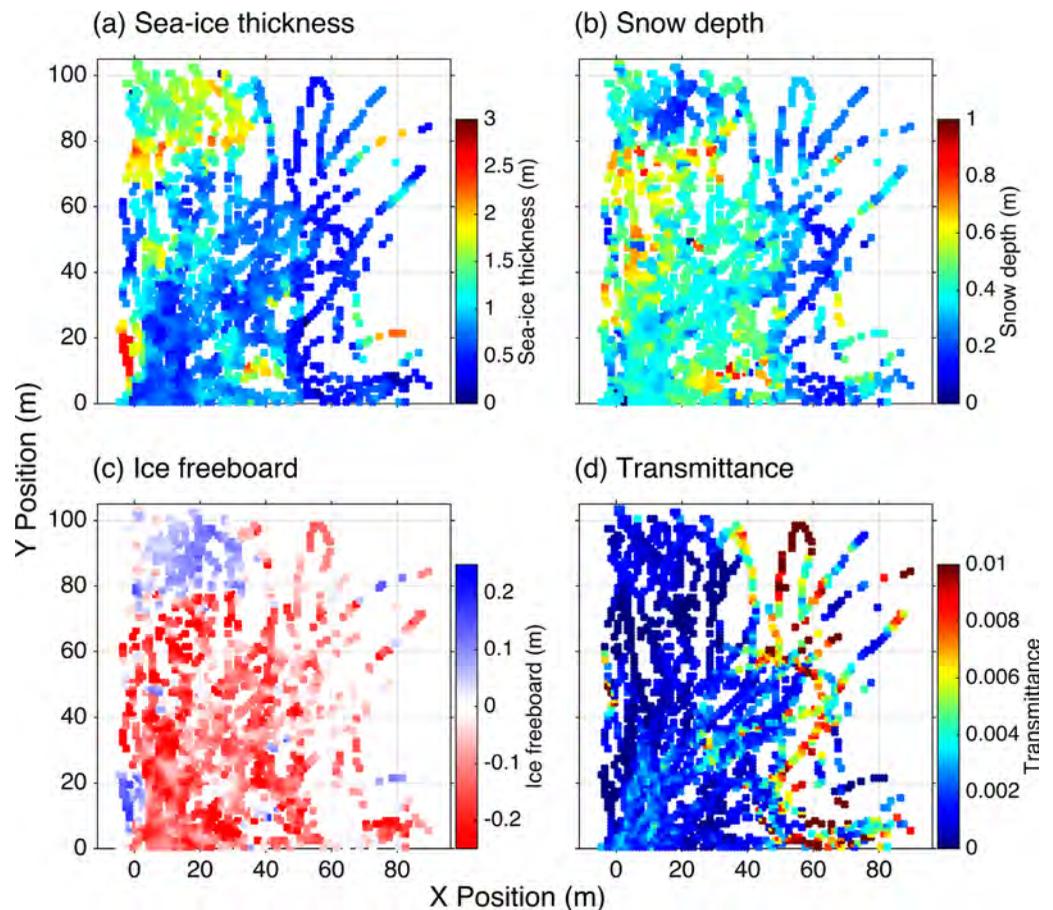
Figure 3. Physical properties of the ice floe within the Remotely Operated Vehicle (ROV) survey area. (a) Sea-ice thickness derived from the ground-based multifrequency electromagnetic induction instrument (GEM-2). (b) Snow depth measured with the Magna Probe. (c) Ice freeboard estimated from equation (1). (d) Light transmittance derived as the ratio of measured transmitted irradiance and incoming solar irradiance above the surface. Sea-ice thickness and snow depth measurements as well as ice freeboard are interpolated to the ROV transect lines. All data are gridded to a 2m-by-2m grid.
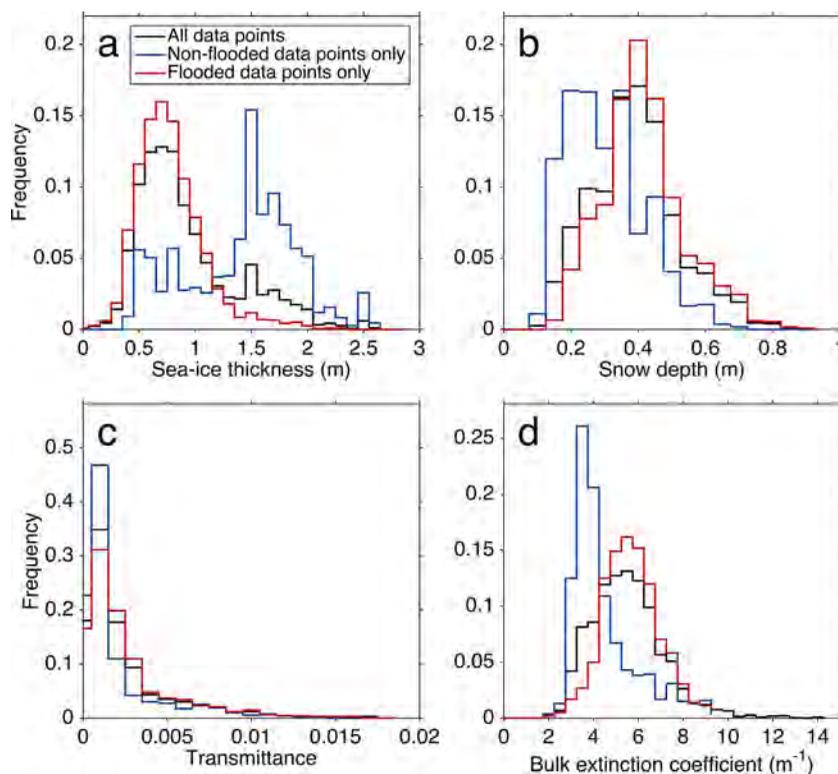
Figure 4. Histograms of (a) sea-ice thickness, (b) snow depth, (c) light transmittance, and (d) calculated bulk light extinction coefficients for the entire data set (black), nonflooded data points only (blue), and flooded data points only (red).

floe show a mean ice thickness and snow depth of 1.00 ± 0.48 m and 0.38 ± 0.15 m, respectively (S2). Considering the ROV grid only, which measured approximately 100 m-by-100 m, the mean sea-ice thickness decreased to 0.93 ± 0.45 m with an additional snow layer of 0.39 ± 0.13 m (Table 1). The estimated ice freeboard reveals that 77% of the surface layer in the ROV grid is assumed to be flooded with a maximum negative freeboard of up to 0.40 m (equation (1.2), Figure 3c, and Table 1). Excluding the flooded grid cells, the mode of the GEM2-derived sea-ice thickness distribution shifts toward higher values, from 0.7 m (all data points) to 1.5 m (nonflooded data points only, Figure 4a). The snow depth distribution has a modal value of 0.25 m for nonflooded data points and 0.4 m for the entire data set, respectively (Figure 4b). Also the mean snow depth is lower for nonflooded data points compared to flooded ones (0.30 ± 0.12 m and 0.42 ± 0.12 m, Table 1). This is expected, as thicker sea ice and less snow are clear indicators for nonflooded sea ice.

While the incoming solar radiation reached values between 90 and 260 Wm^{-2}, only a small fraction ranging between almost 0 and 5 Wm^{-2} was transmitted to the upper ocean (S3). The light transmittance distribution shows a modal value of 0.0008 (0.08%) for the entire data set (Figure 4c and Table 1). The right part of the ROV-grid ($x > 40$ m, Figure 3d) is dominated by a stronger variability in the light transmittance with values up to 0.05 (5%) leading to an overall mean light transmittance of 0.0024 ± 0.0030 ($0.24 \pm 0.30\%$). Distinguishing for flooded and non-flooded data points, the modal transmittance values remain both at 0.0008 (0.08%). In contrast, considering flooded areas only (Figure 3d and Table 1) the average transmittance shifts toward 0.0026 ± 0.0031 ($0.26 \pm 0.31\%$). Nonflooded areas show a lower averaged transmittance of 0.0019 ± 0.0025 ($0.19 \pm 0.25\%$).

3.2. Light Attenuation

Relating the (bulk) light transmittance to both sea-ice thickness and snow depth requires a multidimensional exponential model (equation (3.1)). Single snow and ice extinction coefficients were computed for both the entire data set and the subsets of flooded and nonflooded data points only. Analyzing the entire data set results in bulk extinction coefficients of 6.829 ± 0.045 m^{-1} and 7.737 ± 0.049 m^{-1} for sea ice and snow. The extinction coefficient for sea ice seems to be extremely high (expected between 0.8 and 1.5 m^{-1}) [*Light*
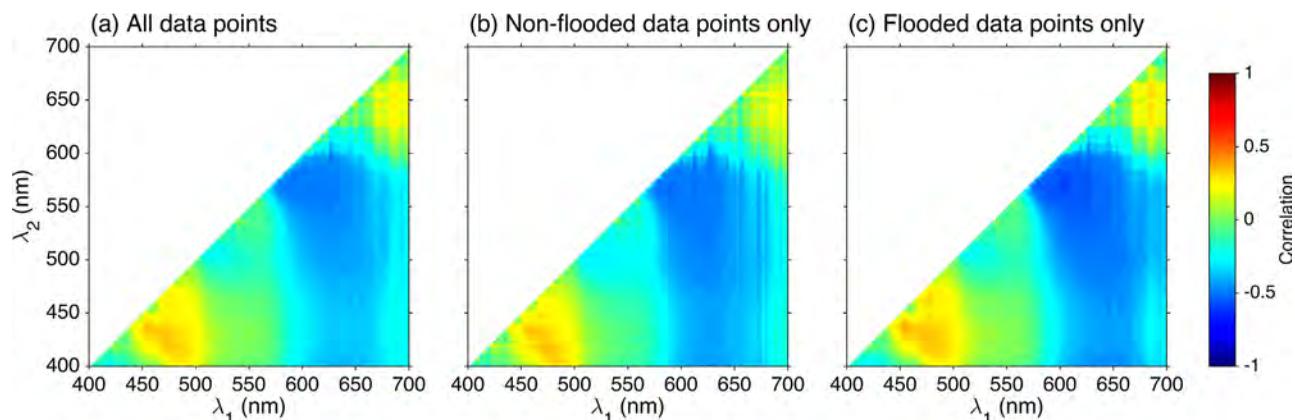
Figure 5. Correlation surfaces of normalized difference indices (NDI) for snow depth for (a) all data points, (b) nonflooded data points only, and (c) flooded data points only. λ_1 and λ_2 indicate the used wavelength pairs according to equation (4).

et al., 2008; Perovich, 1996] and for snow comparable low (expected between 10 and 100 m^{-1}) [Perovich, 2007; Warren, 1982]. The analysis shows that only 65% of variance in the under-ice light field can be explained by sea-ice thickness and snow depth. Extending the model toward a third component for the snow-slush layer on flooded areas only (equation (3.2)), the exponential fit explains still only 61% of the light transmittance variations and leads to extinction coefficients of 2.06 ± 0.97 m^{-1}, 6.21 ± 3.23 m^{-1}, and 31.22 ± 0.53 m^{-1} for sea ice, the flooding layer, and snow, respectively (Table 1). In contrast, fitting non-flooded data points only results in extinction coefficients for sea ice and snow differing by one order of magnitude, 1.264 ± 0.133 m^{-1} (sea ice) and 31.76 ± 0.69 m^{-1} (snow) and the exponential fit explains 74% of the light transmittance variations. These extinction coefficients are much more realistic and compare well with previously reported values [e.g., Grenfell and Maykut, 1977; Perovich, 1996, 2007].

Bulk light extinction coefficients calculated from bulk light transmittance and total ice thickness (sea-ice thickness plus snow depth, equation (2)) show a unimodal distribution for both the entire data set and the chosen subsets (Figure 4d). The modal bulk extinction coefficient for the entire data set and the flooded data points is 5.5 m^{-1}, whereas bulk extinction coefficients are lower for nonflooded data points with a distinct modal value at 3.75 m^{-1}. The tail of the distribution is longer (maximum 14 m^{-1}) for the entire data set than for the nonflooded data points only (maximum 10 m^{-1}).

3.3. Spectral Correlation Surfaces

Figure 5 shows the correlation surfaces of normalized difference indices (NDIs) for snow depth, which shows distinct changes between positive and negative correlations along the diagonal at approximately 440, 580, and 670 nm for both the entire data set and the nonflooded data points only. These sign changes are due to inflection points in the spectral attenuation and absorption of impurities (ice algae) and snow [Perovich, 1996], the almost linear increase in snow attenuation from 570 nm leads to a negative correlation coefficient [Mundy et al., 2007].

The correlations between the NDIs and snow depth are quite weak with correlation coefficients of 0.49, 0.52, and 0.57 for the entire data set, nonflooded, and flooded data points only, respectively. The highest absolute correlations were found at wavelength pairs of 613:581 nm (entire data set) and 613:580 nm (non-flooded data points only) while the one for flooded tends toward lower wavelengths (601:570 nm). The weakest pronounced effect of snow on the transmitted spectral irradiance is shown at wavelengths between 400 and 570 nm, and 620 and 700 nm, which can be associated with the prevalent biomass absorption in these wavelength bands [Ficek et al., 2004].

3.4. Spectral Light Attenuation and Transmission

Figure 6 shows the mean spectral transmitted irradiance, light transmittance, and bulk extinction coefficients for the examined survey area distinguished for flooded and nonflooded areas (Figures 6a, 6c, and 6e) as well as subdivided into snow depth classes, one smaller than 0.2 m and the other one between 0.2 and 0.4 m for an equal sea-ice thickness of 0.8 to 1 m (Figures 6b, 6d, and 6f).
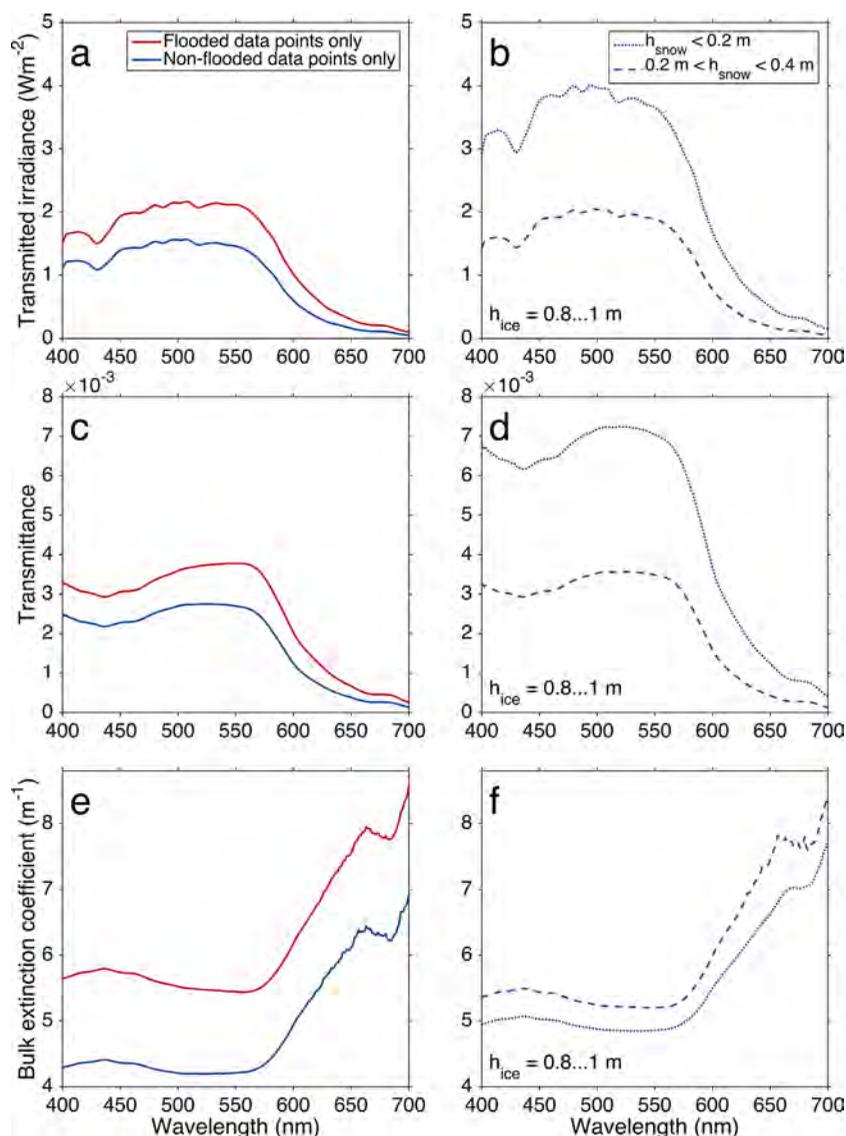
Figure 6. Mean spectral (a and b) transmitted irradiance, (c and d) light transmittance, and (e and f) bulk extinction coefficient for (a, c, e) flooded data points only (red), nonflooded data points only (blue) and (b, d, f) nonflooded data points only with a sea-ice thickness between 0.8 and 1 m subdivided into two snow classes: snow depth < 0.2 m (dotted lines) and snow depth > 0.2 m and < 0.4 m (dashed lines).

Flooded and nonflooded areas reveal the same spectral shape for transmitted irradiance, bulk light transmission, and bulk extinction coefficients, with flooded transmittance and under-ice irradiance values being slightly larger (Figure 6a). Extinction coefficients at PAR wavelengths were about 30% larger for flooded and denser snow than for nonflooded areas (Figure 6c). In both cases, the largest spectral light transmittance and smallest spectral bulk extinction coefficient were found between 470 and 570 nm. The absolute spectral minimum shifts from 520 nm for nonflooded data points to 550–560 nm for flooded data points, most likely as a result of increasing impurities in the slush layer. Moreover, transmitted irradiance and light transmittance decreases with increasing snow depth (Figure 6b), and thus increasing scattering in the snowpack. The spectral under-ice irradiance field and bulk extinction coefficients indicate less wavelength dependence below than above wavelengths of 570 nm. For wavelengths beyond 570 nm, light attenuation follows an almost linear increase (Figure 6d), a typical feature of higher ice absorption at longer wavelengths, which implicates a prominent decrease in the spectral transmitted irradiance and light transmittance (Figure 6b). Even though the absolute correlation coefficients with snow increase in the same wavelength range, the correlation is not significant (Figure 5), indicating the low spectral dependency of snow attenuation

[*Perovich*, 1996]. Our results for nonflooded data points only show a steeper decrease in transmittance and irradiance for thinner than thicker snow at wavelengths beyond 570 nm (Figure 6b), and therefore also higher correlation coefficients (Figure 5b). Nevertheless, the maximum correlation of 0.52 at 614:518 nm is still not substantial for a suitable relation between snow depth and NDI.

4. Discussion

4.1. Spatial Variability of the Under-ice Radiation

The presented case study shows an overall dark under-ice light regime for austral spring (September) Weddell Sea pack ice with a modal light transmittance below 0.1%. Our study also illustrates the importance to distinguish between flooded and nonflooded areas when relating the spatial variability of optical properties to Antarctic sea-ice characteristics. The results from nonflooded grid cells show high extinction coefficients for snow (31.76 ± 0.69 m^{-1}, section 3.3) revealing a strong scattering in the respective snowpack. Since Antarctic sea ice is covered with snow during most of the year [*Massom et al.*, 2001], seasonal snowmelt processes [*Arndt et al.*, 2016] lead to a snowpack consisting of highly compacted and metamorphic layers of snow with internal ice layers [*Nicolaus et al.*, 2009]. This highly inhomogeneous snowpack and density structure leads to weak observed correlations of transmitted solar radiation with snow depth (Figure 5). In contrast, sea-ice in the marginal-ice zone (MIZ) is expected to have a younger and less metamorphous snow layer compared to our studied pack-ice floe. Thus, point-measurements during WWOS in austral spring 2006 and the SIPEX voyages during austral spring 2007 and 2012 in the MIZ (see Section 1) show strong correlations between light transmittance and snow depth. The more homogeneous snowpack in the area leads to correlation coefficients of up to 0.744 and 0.789, respectively [*Melbourne-Thomas et al.*, 2015].

Regarding flooding areas, an additional layer of water-saturated snow needs to be considered. Although slush may contain more light-absorbing impurities, it has less interfaces than snow and is therefore expected to reveal a reduced scattering, and thus has an extinction coefficient much lower than the one of snow (6.21 ± 3.23 m^{-1} versus 31.22 ± 0.53 m^{-1}). High uncertainties of the estimated extinction coefficients might be related to the complex and not quantified geometry of the slush layer. Moreover, the calculated extinction coefficient of sea ice is slightly higher for flooded than for nonflooded areas (2.06 ± 0.97 m^{-1} versus 1.26 ± 0.13 m^{-1}). This might be explained by a combination of several factors: Flooded sea ice is expected to have higher snow loads (Figure 4b) translating directly into increasing extinction compared to nonflooded areas. In contrast, the flooded snow layer (slush) has a different geometry related to less scattering and lower extinction coefficients. However, since flooding is caused by sea water penetrating from the ocean/ice to the snow/ice interface, flooded sea ice is expected to have more impurities leading to an increased scattering and absorption. Overall, the combination of the different geometry of sea ice, slush, and snow leads to slightly higher bulk extinction coefficients of flooded compared to nonflooded areas.

Moreover, snow-slush is expected to refreeze rapidly and form subsequent snow-ice at the sea-ice surface. Consequently, the horizontal and vertical inhomogeneous distributions of snow, slush, and snow-ice at the sea-ice surface prevent a more detailed description of the flooded sea-ice and snow column. Nevertheless, changing physical properties of flooded snow, as e.g., higher densities, emphasizes dominant scattering processes in the flooded (thicker) snowpack, which drive the magnitude of the extinction coefficient and the related transmittance [*Perovich*, 1996]. In contrast, the wavelength-dependence of flooded and nonflooded areas is similar indicating a similar absorption behavior for both media.

Our case study on one pack-ice floe demonstrates that the spatial variability of light levels of the Antarctic under-ice light regime is driven by the presence of surface flooding on scales of smaller than 100 m-by-100 m. Nevertheless, physical properties that determine the light transmittance on a local scale are rather internal layer properties and snow metamorphism, and therefore prevent a direct correlation of light transmittance and snow depth only. On larger scales, features of higher light transmittance, as e.g., leads and breaks between the ice floes (lateral incidence of light), dominate the under-ice light field, as studied during a recent field campaign in the Weddell Sea [*Boebel*, 2015]. Consequently, the entire vertical light profile in the upper ocean must be considered, as the light maximum might not occur at the ice-ocean interface but in deeper layers [*Frey et al.*, 2011; *Katlein et al.*, 2016]. The broad variety and abundance of organisms in

the ice-covered Southern Ocean also supports the notion of sufficient light availability in the upper ocean [*Taylor et al.*, 2013].

To quantify relations of physical properties of the snowpack and underlying sea ice, more studies of the under-ice light field are necessary, not only in the pack ice but also in the marginal sea-ice zone. The latter is expected to reveal different relationships between surface properties and the light regime in the upper ocean, compared to the (inner) pack ice.

4.2. Comparison to Arctic Light Transmittance

Arctic and Antarctic sea-ice areas are known as being rather different—not only regarding their opposing evolution in sea-ice extent during the last decades [*Stammerjohn et al.*, 2012] but particularly in their distinctly different dominant surface properties in spring and summer. Snow on Arctic sea ice melts during the spring-summer transition [*Markus et al.*, 2009], leading to a subsequently widespread ponding of the sea-ice surface [*Rösel and Kaleschke*, 2012; *Webster et al.*, 2015]. In contrast, snow on Antarctic sea ice persists year-round [*Massom et al.*, 2001] with diurnal freeze-thaw cycles at the snow surface modifying the physical properties of the entire snowpack [*Willmes et al.*, 2009; *Arndt et al.*, 2016], most evident by the formation of ice lenses and superimposed ice at the snow/ice interface [*Nicolaus et al.*, 2009]. A main difference between the snow cover in both hemispheres results from the different dominant ablation processes. Arctic snow is dominated by snow melt resulting in the formation of melt ponds and from liquid water, while sublimation on Antarctic sea ice removes most snow as water vapor into the atmosphere [*Nicolaus et al.*, 2006]. Thicker snow and thinner ice in the Antarctic as compared to Arctic sea ice, result in widespread surface-flooding of Antarctic sea ice which can affect about 15–30% of the Antarctic sea-ice zone [*Arrigo*, 2014 and citations therein]. Flooding is rather rare in the Arctic.

The high cover of Arctic sea ice with seasonal melt ponds causes not only the high amount of transmitted solar radiation during summer [*Arndt and Nicolaus*, 2014; *Hudson et al.*, 2013; *Nicolaus et al.*, 2012] but also drives the spatial variability of the under-ice light field on scales smaller 1000 m^2 [*Katlein et al.*, 2015]. While the transmittance of bare first-year (multiyear) ice reaches 4 (1)% during Arctic summer, it increases for ponded first-year (multi-year) ice up to 22 (15)% [*Arndt and Nicolaus*, 2014; *Nicolaus et al.*, 2012]. Considering larger areas, *Katlein et al.* [2015] describe variations in sea-ice thickness as indicator for the variability in the Arctic light transmission. In contrast, the present study indicates that snow depth and flooding are key variables controlling the magnitude and spatial distribution of the Antarctic under-ice light field on scales smaller than 10000 m^2.

Our results suggest that, due to the highly heterogeneous quality of the snowpack, the impact of snow depth on the Antarctic under-ice light field cannot be extrapolated to larger scales without additional in situ information. Instead, a future Antarctic-wide upscaling of light transmittance will need to consider the history and thus former melt processes of the snowpack in every single grid cell. This may then allow an estimate of internal physical properties as well as the quantification of, e.g., metamorphous snow layers and ice lenses [*Arndt et al.*, 2016]. To account for seasonal changes in the Antarctic snowpack, local observations from autonomous systems, as e.g., snow or ice-mass balance buoys, can be used [*Maksym et al.*, 2012]. The annual cycle of processes at the snow/ice interface, as e.g., surface flooding, snow-ice formation, or superimposed ice formation, can be derived from radar backscatter data [*Haas*, 2001], since comprehensive field observations are not feasible. Recent studies on snow depth and ice thickness observations from radar and passive microwave sensors allow for an additional Antarctic-wide estimation of sea-ice freeboard and related quantification of sea-ice surface flooding [*Kern and Ozsoy-Çiçek*, 2016; *Kern et al.*, 2016]. In contrast, the distinct seasonal cycle of Arctic surface properties and more homogeneous vertical snowpack properties allow the parameterization of Arctic-wide light transmittance during all seasons [*Arndt and Nicolaus*, 2014].

5. Conclusions

This case study presents first measurements of the spatial variability of under-ice light transmission connected to measurements of spatially varying surface properties of an Antarctic pack ice floe. An improved understanding of optical properties of Antarctic sea ice and the quantification of light penetrating through sea ice into the upper ocean are needed to further understanding of the timing and amount of interior sea-ice melt (sea-ice mass balance) as well as under-ice ecosystem dynamics.

Even though the amount of light transmission through Antarctic sea ice is low ($<0.1\%$) during austral spring, we were able to identify key processes determining the spatial variation of the under-ice light field. While the distinction between flooded and nonflooded sea-ice regimes dominates the spatial scales of under-ice variability for areas smaller than 100 m-by-100 m, a distinct relation between Antarctic surface properties and the under-ice light field appears not feasible. Although the strong scattering of the thicker snowpack in flooded areas yields a higher attenuation, the dominant heterogeneous snowpack prevents the description of optical properties as a function of snow depth only. In contrast, the Arctic under-ice light field can be directly quantified from sea-ice properties, e.g., sea-ice type and melt pond coverage [*Hudson et al.*, 2013; *Katlein et al.*, 2015; *Nicolaus et al.*, 2012]. Combining surface properties with Arctic-wide remote sensing data, has allowed upscaling of the under-ice light regime for all seasons [*Arndt and Nicolaus*, 2014]. Performing a similar upscaling for Antarctic sea ice requires a more extensive approach. First, an analysis of the temporal evolution of the snowpack from microwave remote sensing observations is needed [*Arndt et al.*, 2016; *Haas*, 2001]. This would allow for a better quantification of the amount of metamorphous snow layers and ice lenses in the prevalent snowpack. Second, we suggest a more detailed analysis of the vertical snow structure associated with light transmission measurements for future field work. The combination of sea-ice thickness, snow depth, and its stratigraphy with under-ice solar radiation measurements will contribute to a better understanding of snow/ice interface processes which, according to our study, will be key to understand transmission and for potential Antarctic-wide upscaling approaches of the under-ice light.

References

Arndt, S., and M. Nicolaus (2014), Seasonal cycle and long-term trend of solar energy fluxes through Arctic sea ice, *Cryosphere*, *8*(6), 2219–2233, doi:10.5194/tc-8-2219-2014.

Arndt, S., S. Willmes, W. Dierking, and M. Nicolaus (2016), Timing and regional patterns of snowmelt on Antarctic sea ice from passive microwave satellite observations, *J. Geophys. Res. Oceans*, *121*, 5916–5930, doi:10.1002/2015JC011504.

Arrigo, K. R. (2014), Sea ice ecosystems, *Annu. Rev. Mar. Sci.*, *6*, 439–467, doi:10.1146/annurev-ma-7-120414-100001.

Arrigo, K. R., et al. (2012), Massive phytoplankton blooms under arctic sea ice, *Science*, *336*(6087), 1408–1408, doi:10.1126/science.1215065.

Belzile, C., S. C. Johannessen, M. Gosselin, S. Demers, and W. L. Miller (2000), Ultraviolet attenuation by dissolved and particulate constituents of first-year ice during late spring in an Arctic polynya, *Limnol. Oceanogr.*, *45*(6), 1265–1273, doi:10.4319/lo.2000.45.6.1265.

Boebel, O. (2015), The Expedition PS89 of the Research Vessel POLARSTERN to the Weddell Sea in 2014/2015, in *Berichte zur Polar-und Meeresforschung= Reports On Polar and Marine Research*, vol. 689, Alfred Wegener Institute for Polar and Marine Research, Bremerhaven, Germany.

Brandt, R. E., S. G. Warren, A. P. Worby, and T. C. Grenfell (2005), Surface albedo of the Antarctic sea ice zone, *J. Clim.*, *18*(17), 3606–3622, doi:10.1175/jcli3489.1.

Campbell, K., C. J. Mundy, D. G. Barber, and M. Gosselin (2015), Characterizing the sea ice algae chlorophyll a-snow depth relationship over Arctic spring melt using transmitted irradiance, *J Mar. Syst*, *147*, 76–84, doi:10.1016/j.jmarsys.2014.01.008.

Eicken, H., M. A. Lange, H. W. Hubberten, and P. Wadhams (1994), Characteristics and distribution patterns of snow and meteoric ice in the Weddell Sea and their contribution to the mass balance of sea ice, *Ann. Geophys.*, *12*(1), 80–93, doi:10.1007/s00585-994-0080-x.

Ficek, D., S. Kaczmarek, J. Ston-Egiert, B. Wozniak, R. Majchrowski, and J. Dera (2004), Spectra of light absorption by phytoplankton pigments in the Baltic; conclusions to be drawn from a Gaussian analysis of empirical data, *Oceanologia*, *46*(4), 533–555.

Frey, K. E., D. K. Perovich, and B. Light (2011), The spatial distribution of solar radiation under a melting Arctic sea ice cover, *Geophys. Res. Lett.*, *38*, L22501, doi:10.1029/2011GL049421.

Fritsen, C. H., E. D. Wirthlin, D. K. Momberg, M. J. Lewis, and S. F. Ackley (2011), Bio-optical properties of Antarctic pack ice in the early austral spring, *Deep Sea Res., Part II*, *58*(9-10), 1052–1061, doi:10.1016/j.dsr2.2010.10.028.

Grenfell, T. C., and G. A. Maykut (1977), The optical properties of ice and snow in the Arctic Basin, *J. Glaciol.*, *18*(80), 445–463, doi:10.3198/1977JoG18-80-445-463.

Haas, C. (2001), The seasonal cycle of ERS scatterometer signatures over perennial Antarctic sea ice and associated surface ice properties and processes, *Ann. Glaciol.*, *33*, 69–73, doi:10.3189/172756401781818301.

Haas, C., D. N. Thomas, and J. Bareiss (2001), Surface properties and processes of perennial Antarctic sea ice in summer, *J. Glaciol.*, *47*(159), 613–625, doi:10.3189/172756501781831864.

Hudson, S. R., M. A. Granskog, A. Sundfjord, A. Randelhoff, A. H. H. Renner, and D. V. Divine (2013), Energy budget of first-year Arctic sea ice in advanced stages of melt, *Geophys. Res. Lett.*, *40*, 2679–2683, doi:10.1002/grl.50517.

Hunkeler, P. A., S. Hendricks, M. Hoppmann, S. Paul, and R. Gerdes (2015), Towards an estimation of sub-sea-ice platelet-layer volume with multi-frequency electromagnetic induction sounding, *Ann. Glaciol.*, *56*(69), 137–146.

Hunkeler, P. A., S. Hendricks, M. Hoppmann, C. G. Farquharson, T. Kalscheuer, M. Grab, M. S. Kaufmann, L. Rabenstein, and R. Gerdes (2016), Improved 1D inversions for sea ice thickness and conductivity from electromagnetic induction data: Inclusion of nonlinearities caused by passive bucking, *Geophysics*, *81*(1), Wa45–Wa58, doi:10.1190/geo2015-0130.1.

Katlein, C., et al. (2015), Influence of ice thickness and surface properties on light transmission through Arctic sea ice, *J. Geophys. Res. Oceans*, *120*, 5932–5944, doi:10.1002/2015JC010914.

Katlein, C., D. K. Perovich, and M. Nicolaus (2016), Geometric Effects of an Inhomogeneous Sea Ice Cover on the under Ice Light Field, *Front. Earth Sci.*, *4*, 6.

Kern, S., and B. Ozsoy-Çiçek (2016), Satellite remote sensing of snow depth on Antarctic Sea Ice: An inter-comparison of two empirical approaches, *Remote Sens.*, *8*(6), 450, doi:10.3390/rs8060450.

Kern, S., B. Ozsoy-Çiçek, and A. P. Worby (2016), Antarctic Sea-Ice Thickness Retrieval from ICESat: Inter-Comparison of Different Approaches, *Remote Sens.*, *8*(7), 538, doi:10.3390/rs8070538.

Knight, C. A. (1988), Formation of slush on floating ice, *Cold Reg. Sci. Technol.*, *15*(1), 33–38.

Lange, M. A., P. Schlosser, S. F. Ackley, P. Wadhams, and G. S. Dieckmann (1990), O-18 concentrations in sea ice of the Weddell Sea, Antarctica, *J. Glaciol.*, *36*(124), 315–323, doi:10.3189/002214390793701291.

Lemke, P. (2009), The expedition of the research vessel "Polarstern" to the Antarctic in 2006 (ANT-XXIII/7), in *Berichte zur Polar-und Meeresforschung (Reports on Polar and Marine Research)*, vol. 586, Alfred Wegener Institute for Polar and Marine Research, Bremerhaven, Germany.

Light, B., T. C. Grenfell, and D. K. Perovich (2008), Transmission and absorption of solar radiation by Arctic sea ice during the melt season, *J. Geophys. Res.*, *113*, C03023, doi:10.1029/2006JC003977.

Maksym, T., S. E. Stammerjohn, S. Ackley, and R. Massom (2012), Antarctic sea Ice-A polar opposite?, *Oceanography*, *25*(3), 140–151, doi: 10.5670/oceanog.2012.88.

Markus, T., J. C. Stroeve, and J. A. Miller (2009), Recent changes in Arctic sea ice melt onset, freezeup, and melt season length, *J. Geophys. Res.*, *114*, C12024, doi:10.1029/2009JC005436.

Massom, R. A., and S. E. Stammerjohn (2010), Antarctic sea ice change and variability–physical and ecological implications, *Polar Sci.*, *4*(2), 149–186, doi:10.1016/j.polar.2010.05.001.

Massom, R. A., et al. (2001), Snow on Antarctic Sea ice, *Rev. Geophys.*, *39*(3), 413–445, doi:10.1029/2000RG000085.

Meiners, K. M., K. M. Golden, P. Heil, J. L. Lieser, R. Massom, B. Meyer, and G. D. Williams (2016), Introduction: SIPEX-2: A study of sea-ice physical, biogeochemical and ecosystem processes off East Antarctica during spring 2012, *Deep Sea Res., Part II*, *131*, 1–6, Topical Studies in Oceanography, doi:10.1016/j.dsr2.2016.06.010.

Melbourne-Thomas, J., K. M. Meiners, C. Mundy, C. Schallenberg, K. L. Tattersall, and G. S. Dieckmann (2015), Algorithms to estimate Antarctic sea ice algal biomass from under-ice irradiance spectra at regional scales, *Mar. Ecol. Prog. Ser.*, *536*, 107–121, doi:10.3354/meps11396.

Meyer, B., and L. Auerswald (2014), The expedition of the research vessel "Polarstern" to the Antarctic in 2013 (ANT-XXIX/7), in *Berichte zur Polar-und Meeresforschung = Reports on Polar and Marine Research*, vol. 674, Alfred Wegener Institute for Polar and Marine Research, Bremerhaven, Germany.

Michael, K. J., and J. Higgins (2014), Diffuse Attenuation coefficients for east Antarctic Pack Ice and snow at ultraviolet and visible wavelengths, *IEEE Trans. Geosci. Remote Sens.*, *52*(7), 4455–4461, doi:10.1109/TGRS.2013.2282158.

Mundy, C. J., D. G. Barber, and C. Michel (2005), Variability of snow and ice thermal, physical and optical properties pertinent to sea ice algae biomass during spring, *J Mar. Syst.*, *58*(3–4), 107–120, doi:10.1016/j.jmarsys.2005.07.003.

Mundy, C. J., J. K. Ehn, D. G. Barber, and C. Michel (2007), Influence of snow cover and algae on the spectral dependence of transmitted irradiance through Arctic landfast first-year sea ice, *J. Geophys. Res.*, *112*, C03007, doi:10.1029/2006JC003683.

Nicolaus, M., and C. Katlein (2013), Mapping radiation transfer through sea ice using a remotely operated vehicle (ROV), *Cryosphere*, *7*(3), 763–777, doi:10.5194/tc-7-763-2013.

Nicolaus, M., C. Haas, and J. Bareiss (2003), Observations of superimposed ice formation at melt-onset on fast ice on Kongsfjorden, Svalbard, *Phys. Chem. Earth*, *28*(28–32), 1241–1248, doi:10.1016/j.pce.2003.08.048.

Nicolaus, M., C. Haas, J. Bareiss, and S. Willmes (2006), A model study of differences of snow thinning on Arctic and Antarctic first-year sea ice during spring and summer, *Ann. Glaciol.*, *44*, 147–153.

Nicolaus, M., C. Haas, and S. Willmes (2009), Evolution of first-year and second-year snow properties on sea ice in the Weddell Sea during spring-summer transition, *J. Geophys. Res.*, *114*, D17109, doi:10.1029/2008JD011227.

Nicolaus, M., S. R. Hudson, S. Gerland, and K. Munderloh (2010), A modern concept for autonomous and continuous measurements of spectral albedo and transmittance of sea ice, *Cold Reg. Sci. Technol.*, *62*(1), 14–28, doi:10.1016/j.coldregions.2010.03.001.

Nicolaus, M., C. Katlein, J. Maslanik, and S. Hendricks (2012), Changes in Arctic sea ice result in increasing light transmittance and absorption, *Geophys. Res. Lett.*, *39*, L24501, doi:10.1029/2012GL053738.

Perovich, D. K. (1996), The optical properties of sea ice, report, 25 p, U.S. Cold Reg. Res. and Eng. Lab. Monogr., Hannover, N. H.

Perovich, D. K. (2007), Light reflection and transmission by a temperate snow cover, *J. Glaciol.*, *53*(181), 201–210, doi:10.3189/172756507782202919.

Perovich, D. K., C. S. Roesler, and W. S. Pegau (1998), Variability in Arctic sea ice optical properties, *J. Geophys. Res.*, *103*(C1), 1193–1208, doi:10.1029/97JC01614.

Perovich, D. K., K. F. Jones, B. Light, H. Eicken, T. Markus, J. Stroeve, and R. Lindsay (2011), Solar partitioning in a changing Arctic sea-ice cover, *Ann. Glaciol.*, *52*(57), 192–196, doi:10.3189/172756411795931543.

Rösel, A., and L. Kaleschke (2012), Exceptional melt pond occurrence in the years 2007 and 2011 on the Arctic sea ice revealed from MODIS satellite data, *J. Geophys. Res.*, *117*, C05018, doi:10.1029/2011JC007869.

Stammerjohn, S., R. Massom, D. Rind, and D. Martinson (2012), Regions of rapid sea ice change: An inter-hemispheric seasonal comparison, *Geophys. Res. Lett.*, *39*, L06501, doi:10.1029/2012GL050874.

Sturm, M., and R. A. Massom (2010), Snow and sea ice, in *Sea Ice*, 2nd ed., edited by D. N. Thomas and G. S. Dieckmann, pp. 153–204, Wiley-Blackwell, Oxford, U. K., doi:10.1002/9781444317145.ch5.

Taylor, M. H., M. Losch, and A. Bracher (2013), On the drivers of phytoplankton blooms in the Antarctic marginal ice zone: A modeling approach, *J. Geophys. Res. Oceans*, *118*, 63–75, doi:10.1029/2012JC008418.

Uusikivi, J., A. V. Vahatalo, M. A. Granskog, and R. Sommaruga (2010), Contribution of mycosporine-like amino acids and colored dissolved and particulate matter to sea ice optical properties and ultraviolet attenuation, *Limnol. Oceanogr.*, *55*(2), 703–713, doi:10.4319/lo.2009.55.2.0703.

Warren, S. G. (1982), Optical properties of snow, *Rev. Geophys.*, *20*(1), 67–89, doi:10.1029/RG020i001p00067.

Webster, M. A., I. G. Rigor, D. K. Perovich, J. A. Richter-Menge, C. M. Polashenski, and B. Light (2015), Seasonal evolution of melt ponds on Arctic sea ice, *J. Geophys. Res. Oceans*, *120*, 5968–5982, doi:10.1002/2015JC011030.

Williams, G. D., et al. (2013), Beyond point measurements: Sea ice floes characterized in 3-D, *Eos Trans. AGU*, *94*(7), 69–70, doi:10.1002/2013EO070002.

Willmes, S., C. Haas, M. Nicolaus, and J. Bareiss (2009), Satellite microwave observations of the interannual variability of snowmelt on sea ice in the Southern Ocean, *J. Geophys. Res.*, *114*, C03006, doi:10.1029/2008JC004919.

Worby, A. P., A. Steer, J. L. Lieser, P. Heil, D. H. Yi, T. Markus, I. Allison, R. A. Massom, N. Galin, and J. Zwally (2011), Regional-scale sea-ice and snow thickness distributions from in situ and satellite measurements over East Antarctica during SIPEX 2007, *Deep Sea Res., Part II*, *58*(9–10), 1125–1136, doi:10.1016/j.dsr2.2010.12.001.

Yi, D., H. J. Zwally, and J. W. Robbins (2011), ICESat observations of seasonal and interannual variations of sea-ice freeboard and estimated thickness in the Weddell Sea, Antarctica (2003–2009), *Ann. Glaciol.*, *52*(57), 43–51.